Supporting Information

Transient heating synthesis of highly ordered Ga-Cu intermetallic antiperovskite for efficient ammonia electrosynthesis and ultrastable zinc-nitrate fuel cells

Peifang Wang[a,*], Chongchong Liu[a], Lei Rao[b], Weixiang Tao[a], Rong Huang[a], Peilin Huang[a], Gang Zhou[a,*]

[a] *Key Laboratory of Integrated Regulation and Resource Development on Shallow Lake of Ministry of Education, College of Environment, Hohai University, Nanjing 210098, China*

[b] *College of Materials Science and Engineering, Hohai University, Nanjing 210098, China*

[*] e-mail: pfwang2005@hhu.edu.cn (P. Wang), gangzhou@hhu.edu.cn (G. Zhou).

Table of contents

transient heating temperatures at -0.6 V vs. RHE. (b) The SEM image of Ga-Cu_3N catalysts prepared under 1000 °C.

Figure S8. NH_3 yield rate and FE for Ga-Cu_3N catalysts with different Ga/Cu atomic ratio.

Figure S9. (a) Aberration-corrected HAADF-STEM image of D-Ga-Cu_3N sample. Comparison on (b) Polarization curve, (c) NH_3 yield rate, and (d) Faradaic efficiency of Ga-Cu_3N and D-Ga-Cu_3N catalysts.

Figure S10. (a) ^1H NMR spectra of the $^{15}NH_4Cl$ standards with different content. (b) The corresponding linear standard curve between concentration and peak area. (c) ^1H NMR spectra of the electrolyte after reaction using $^{15}NO_3^-$ as the nitrogen source and the calculated concentration comparison with UV method.

Figure S11. Comprehensive comparison for electrochemical properties of three catalysts.

Figure S12. The obtained Tafel slope from of LSV curves for three catalysts.

Figure S13. CV curves for (a) Cu_3N, (b) V- Cu_3N, and (c) Ga-Cu_3N from 0.8 to 0.9 V versus RHE with various scan rates. (d) Corresponding derived double layer capacitance (Cdl) of samples.

Figure S14. Comparison of (a) SEM, (b) XPS survey spectra, (c) Cu 2p and (d) Ga 3d spectra of Ga-Cu_3N before and after cyclic electrocatalytic tests.

Figure S15. Free energy diagram for H_2O dissociation and *H generation on different sites.

Figure S16. Partial density of states of NO_3^- adsorbed on catalysts. (ε_d: d band center)

Text S1. Preparation of Catalysts

1.1 Chemicals

All involved chemicals are in analytical grade and used without further purifications.

1.2 Synthesis of Cu_3N nanocubes

The preparation of Cu_3N was improved according to a previously reported method [1]. 0.24 mmol of copper nitrate ($Cu(NO_3)_2$) and 7.5 mL of hexadecane ($C_{16}H_{34}$) were dissolved and stirred in a three-neck flask. Then, 2.5 mL of distilled Oleylamine ($C_{18}H_{35}NH_2$) was added and degassed for 30 minutes at 50 °C. Then, the mixture solution was increased to 260 °C at a rate of 10 °C per minute, and react for 15 minutes in argon atmosphere (Ar). The flask was then removed from the heating mantle and left to cool to room temperature over the course of an hour. The 10 mL solution of nanoparticles was removed and added with 15 mL of acetone, centrifuged at 6000 rpm for 4 minutes. The supernatant was removed and the particles were redispersed in 4 mL of cyclohexane and 1 mL of Oleylamine, placed in the ultrasonic bath until fully redispersed. Finally, the mixture (5 mL) was alternatively centrifugated using ethanol (25 mL) and acetone (25 mL) for several times, obtaining the pure Cu_3N nanocubes.

1.3 Synthesis of V-Cu_3N and Ga-Cu_3N.

20 mg of Cu_3N powder, 10 mg of Polyvinylpyrrolidone (PVP), and 8 mg gallium (Ga) were placed in a mortar and ground with a pestle for 15 minutes. The mixture was put on a Tungsten plate (4 cm×2 cm) and moved to the Joule heating device [2]. A

thermal shock was applied to the samples using the sweep function from Keithley where the magnitude (temperature) was set to 800 ℃, and duration (thermal shock time) was 2 s. The obtained samples were alternatively washed by ethanol and water for 3 time to obtain the Ga-Cu_3N catalyst. The V-Cu_3N was prepared via the same heating synthesis method without adding gallium. For comparison, we also fabricated the samples under the heating temperature of 400, 600, and 800 ℃. By changing the added gallium amount into 3, 6 and 12 mg in the transient heating steps, we also prepared $Ga_{0.38}$-Cu_3N, $Ga_{0.75}$-Cu_3N, and $Ga_{0.75}$-Cu_3N catalyst.

1.4 Synthesis of D-Ga-Cu_3N.

The disordered Ga-doped Cu_3N sample (named D-Ga-Cu_3N) was prepared via an ion deposition method. In details, 20 mg of V-Cu_3N and 20.4 mg of Gallium chloride ($GaCl_3$) were dissolved in 4 mL of distilled Oleylamine ($C_{18}H_{35}NH_2$) and stirred in a three-neck flask. Then, the mixture solution was increased to 120 °C at a rate of 10 °C per minute, and react for 30 minutes in argon (Ar) flow. Ga species entered the atomic vacancy on the V-Cu_3N surface with the protection of oleylamine ligands. When cooling to room temperature, the D-Ga-Cu_3N was obtained after alternatively centrifugated using ethanol (25 mL) and acetone (25 mL) for 2 times. The ICP-MS results (Table S2) proved that the synthesized D-Ga-Cu_3N exposed similar elemental distributions with Ga-Cu_3N.

Text S2. Computational Method

The DFT calculation methods on the electronic structure and Gibbs free energy are carried out by first-principles theory via the Vienna Abinitio Simulation Package (VASP) code [3]. The exchange-functional is treated using the generalized gradient approximation (GGA) of Perdew-Burke-Ernzerhof (PBE). The kinetic energy cutoff for the plane wave basis was 450 eV. DFT calculation was established on the single crystal plane of ideal molecular model: (100) for Cu_3N, (111) for V-Cu_3N and (111) for Ga-Cu_3N. Brillouin zone integration on grids with 3×3×1 Monkhorst-Pack k-points was implemented for geometrical optimization and calculation of density of states. The convergence criterion for the electronic self-consistent iteration and force were set to 10^{-5} eV and 0.02 eV/Å. The vacuum layer in the slab model is larger than 15 Å to avoid superficial interaction between periodical slabs and the intermediates were built on the surface for structural relaxation. The free energy (ΔG) of each adsorbed intermediate is calculated as

$$\Delta G = \Delta E + \Delta E_{ZPE} - T\Delta S \quad (1)$$

where ΔE, ΔE_{ZPE}, and ΔS respectively represent the changes of electronic energy, zero-point energy, and entropy that caused by adsorption of intermediate. The thermodynamic corrections at the reaction temperature (300 K) were evaluated by using VASPKIT software [4]. The crystal orbital Hamilton population (COHP) was extracted via the software lobster 4.1.0 [5]. Transition states are searched via the climbing-image nudged elastic band (CI-NEB) method [6], and the threshold value for the forces on each atom was 0.05 eV/Å. Ab initio molecular dynamics (AIMD)

simulations was carried out in the NVT ensemble to test thermodynamically stability [7]. The surface energy calculations were performed in a large-scale atomic/molecular massively parallel simulator (LAMMPS). The temperature was controlled over a Langevin thermostat set and the surface energy was then calculated from the following equation:

$$\gamma(\mathrm{T}) = \frac{E_{slab}(\mathrm{T}) - E_{bulk}(\mathrm{T})}{2\mathrm{A}} \qquad (2)$$

where E_{slab} and E_{bulk} are respectively the potential energies of the separated and bulk material at the given temperature (T). A is the area of the selected crystal surface.

Text S3. Characterization

Crystalline structures were tested on an X-ray diffraction (XRD, Rigaku, SmartLab) with a Cu Kα radiation at a range of 10° to 80° under the operating condition of 40 kV and 100 mA. GSAS-II software was used for the refinements by Rietveld's profile analysis method [8]. The scanning electron morphologies (SEM) were observed on Hitachi S-4800. The TEM images were monitored via JEM 2100Plus, equipped with energy-dispersive X-ray spectrum (Octane SSD, EDAX). Geometric phase analysis (GPA) was conducted on the DigitalMircograph (Gatan) software with FRWR tools plugin. According to the analysis method created by Hÿtch et al. [9], we chose $(\bar{1}01)$ and $(\bar{1}2\bar{1})$ along the zone [111] axis to obtain the in-plane strain (ε_{xx}, $\varepsilon_{yy,}$ ε_{xy}) fields to show the strain distribution. X-ray photoelectron spectroscopy (XPS) patterns were analyzed by an ESCALAB 250Xi+ instrument with a monochromatized Al radiation (Kα = 1486 eV). The X-ray absorption spectra (XAS) were measured at Shanghai Synchrotron Radiation Facility (SSRF), and the data were analyzed by the software Athena and Artemis [10]. All the ultraviolet-visible (UV-vis) spectrum were examined on a Shimadzu UV-3600Plus. Aberration-corrected high-angle annular dark-field scanning transmission electron microscopy (HAADF-STEM) were performed on Thermo Scientific Themis Z. Nuclear magnetic resonance (NMR) spectra were tested on a Bruker 600MHz nuclear magnetic resonance spectrometer. The *In-situ* Raman spectra were obtained on a HORIBA LabRAM HR Evolution under excitation with 532-nm laser light.

Text S4. Electrochemical tests

Electrochemical measurements were tested on an electrochemical work station (CIMPS, Zahner, Germany) with a three-electrode system. The catalyst ink containing 5 mg of sample, 40 μL of Nafion solution (5 wt%), 480 μl of H_2O, and 480 μl of ethanol was sonicated for 40 min, and then 40 μL of ink was dropped on a carbon paper as a working electrode. Its catalytic area was 1.0×1.0 cm^2 and the mass loading was 0.2 mg cm^{-2}. Platinum sheet and Ag/AgCl electrode (filled with saturated KCl) were utilized as counter and reference electrodes, respectively. The electrocatalytic experiments were carried out in a H-type electrolytic cell separated with a Nafion 117 membrane, and the electrolyte was 0.5 M Na_2SO_4 + 0.1 M $NaNO_3$ + 0.1 M PBS (pH= 7) solution (50 mL). The electrolyte was bubbled with high-purity argon (Ar 99.999%) for 0.5 h before the reaction to remove dissolved oxygen. All obtained catalytic potentials in this work were versus Ag/AgCl and transformed to reversible hydrogen electrode (RHE) potential by the following equation:

$$E_{RHE} = E_{Ag/AgCl} + 0.197 + 0.059 \times pH \qquad (3)$$

The NH_3 electrosynthesis was performed in cathode reaction chamber for 1h via a chrono amperometry mode with a steady potential (-0.3, -0.4, -0.5, -0.6, and -0.7 V vs. RHE). The linear sweep voltammetry (LSV) curve was tested with the scan rate of 5 mV s^{-1}. The Tafel slope was obtained by fitting the linear portion of the Tafel plots to the Tafel equation [$\eta = b \log(j)+a$]. The electrochemical impedance spectroscopy (EIS) and Bode plots were recorded at a frequency between 0.1 and 100k Hz under different potentials (0 to -0.9 V vs. RHE). The double layer capacitance (Cdl) was evaluated by

the CV method on the non-faraday region with the scanning rates of 2, 4, 6, 6, 8 and 10 mV s^{-1}. The Cu site poisoning experiment was conducted in the same condition of chrono amperometry mode in addition of adding 0.2 M KSCN. The current density at -0.6 V RHE was collected from LSV curves at different reaction temperature (278 K, 288 K, 298 K, 308 K, and 318 K). Then, the apparent electrochemical activation energy (E_a) for NO_3^-RR was determined by the Arrhenius slope [11]. Turnover frequency (TOF) is defined as the amount of reduction product generated per electrochemically active site per unit time. Herein, the TOF (s^{-1}) was calculated via following formula:

$$TOF = (c_{NH3} \times V) / (17 \times n_{Cu} \times t) \quad (4)$$

where c_{NH3} (mg/L) is the detected NH_3 concentration after chrono amperometry tests at -0.6 V vs. RHE, V (L) is the volume of cathodic electrolyte solution, n_{Cu} (mmol) is the integral molar quantity Cu element on the electrode, which are calculated based on the Cu content from ICP-MS (Table S2) and the catalyst loading, t (s) is the reaction time.

The carbon paper-supported V-Cu_3N or Ga-Cu_3N (catalytic area: 1cm^{-2}) and Zn plate were employed as the cathode and anode, respectively, for flow zinc-nitrate battery. The battery contains 100-mL cathode electrolyte (0.1 M $NaNO_3$ + 0.5 M $NaSO_4$+ 0.1 M PBS (pH= 7)) and 100-mL anode electrolyte (1 M KOH) separated by a bipolar membrane and circulated with a flow rate of 10 mL min^{-1}. Ar gas was purged in the catholyte before the testing to remove any dissolved O_2 and N_2 to avoid the oxygen and nitrogen reduction reaction. The discharging polarization curves with

a scan rate of 5 mV s^{-1} and galvanostatic tests were conducted using electrochemical work station (CIMPS, Zahner, Germany) at room temperature. The powder density for zinc-nitrate battery was determined by P = I×V, where I and V are the discharge current density and voltage, respectively. To recycle NH_3, 100 ml of downstream product was sealed in a flask with 200 sccm Ar gas flowing in for 24 h to perform the air stripping to purge the NH_3 out. The outlet gas stream was purged into 50 ml of 3 M HCl to collect the NH_4Cl product.

The half and overall reaction equations for flow Zn-NO_3^- battery were present as the following:

Cathode reaction: $NO_3^- + 6H_2O + 8e^- \rightarrow NH_3 + 9OH^-$ (5)

Anode reaction: $Zn + 2OH^- \rightarrow ZnO + H_2O + 2e^-$ (6)

Overall reaction: $4Zn + NO_3^- + 2H_2O \rightarrow 4ZnO + NH_3 + OH^-$ (7)

Herein, the half reaction potential for cathode and anode can be calculated by Nernst equation (Eq. 8) [12]:

$$E = E^0 + \frac{RT}{nF} \ln \frac{b(Ox)}{b(Red)} \quad (8)$$

Where E^0 is standard electrode potential (V). The E_0 values for cathode (Eq. 1) and anode (Eq. 2) reactions were -0.12 V and -1.25 V respectively [13–15]. The n, F, R, and T are electron transfer number, the Faraday constant (96485 C mol^{-1}), gas constant (8.314 J mol^{-1} K^{-1}), and reaction temperature (298 K), respectively. [Ox] and [Red] are the concentration (mol L^{-1}) for reaction products, and their exponents are equal to their coefficients in the electrode reaction. Herein, the [NO_3^-] is 0.1 M. The [OH^-] in catholyte and anolyte is 10^{-7} M and 1 M. Assuming the [NH_3] in cathode is 10^{-3} M at

the reaction begging. Hence, we can calculate the theoretical electrode potentials and overall reaction voltage in our Zn-NO_3^- battery system, as seen in Eq. 9-11.

$$E_{cathode} = E^{0}_{cathode} + \frac{RT}{nF} \ln \frac{[NO_3^-]}{[NH_3]\,[OH^-]^9} = 0.35\,V \qquad (9)$$

$$E_{anode} = E^{0}_{anode} + \frac{RT}{nF} \ln \frac{1}{[OH^-]^2} = -1.25\,V \qquad (10)$$

$$E_{overall} = E_{cathode} - E_{anode} = 1.60\ V \qquad (11)$$

Test S5. Determination of products

5.1 Detection of NH_3.

The ammonia concentration in the electrolyte after reaction was determined by the indophenol blue method [16]. First, 2 mL of solution was removed from the electrochemical reaction vessel. Then, 2 mL of NaOH solution (1 M) containing 5 wt% salicylic acid and 5 wt% sodium citrate was added, followed by addition of 1 mL of NaClO (0.05 M) and 0.2 mL of $C_5FeN_6Na_2O$ (sodium nitroferricyanide, 1 wt %). After reacted for 2 h at room temperature, the absorption spectrum was measured using an ultraviolet-visible (UV-Vis) spectrophotometer. The final produced NH_3 content was calibrated based on concentration-absorbance curve at a wavelength of 655 nm. The standard curve can be made by measuring the UV-vis spectra of varied concentrations of $NaNO_3$ solutions. The electrolyte containing NH_3 after reaction was firstly diluted to standard curve range for ammonia tests.

5.2 Detection of NO_3^-.

The concentration of NO_3^- was determined using the UV-Vis spectrophotometry method. After reaction, 1.0 mL electrolyte was removed out of the electrolytic cell and diluted to 5 mL. 0.1 mL HCl (1 M) and 0.01 mL sulfamic acid were further added in the solution. After 20 minutes, the UV-vis absorption spectra were recorded, and the total absorbance of NO_3^- was calculated by the following equation: $A=A_{220}-2*A_{275}$ (where A_{220} and A_{275} are the absorbance coefficients at 220 nm and 275 nm, respectively). The standard curve can be made by measuring the UV-vis spectra of varied concentrations of $NaNO_3$ solutions.

5.3 Detection of NO_2^-.

The nitrite concentration was measured by UV-vis spectrophotometry according to the colorimetric method. Firstly, the color reagent was prepared by mixing sulfonamide (4 g), N-ethylenediamine dihydrochloride (0.2 g), phosphoric acid (H_3PO_4, 10 mL, ρ=1.685 g mL^{-1}), and deionized water (50 ml). The electrolyte sample should be diluted to the detection range. Then 0.1 mL of the color reagent was mixed with 5 mL of the sample solution and rested for 20 min at room condition. The absorption intensity at a wavelength of 540 nm was recorded by UV-Vis absorption spectrum. The concentration of NO_2^- product was calculated based on the calibrated curve, which is linear fitted using a series of standard KNO_2 solutions.

5.4 ^{15}N isotope-labelling ^{1}H NMR

^{1}H NMR spectroscopy (600 MHz) was used to quantify the $^{15}NH_3$ yield after electrolysis using $Na^{15}NO_3$ as reactant at various potentials. The calibration curves with different $^{15}NH_4SO_4$ concentrations were also prepared for concentration calculation. After electroreduction, 200 μl of electrolyte was extracted and then mixed with maleic acid ($C_4H_4O_4$, internal standard) aqueous solution (10 μL, 3.2 mM), H_2SO_4 solution (10 μL, 4 M), and DMSO-d6 (380 μL). All ^{1}H NMR tests were conducted with water suppression, and NH_3 concentration can be determined by comparing the integral area (I) of characteristic peaks with the standards.

5.5 Yield rate and Faraday efficiency

The Faradaic efficiency (FE) and yield rate of NH_3 and NO_2^- can be calculated using the following equation:

$$v_{NH3} = (c_{NH3} \times V)/(t \times S) \quad (5)$$

$$v_{NO_2^-} = (c_{NO_2^-} \times V)/(t \times S) \quad (6)$$

$$FE_{NH3} = (8 \times F \times c_{NH3} \times V)/(M_{NH3} \times Q) \quad (7)$$

$$FE_{NO_2^-} = (6 \times F \times c_{NO_2^-} \times V)/(M_{NO_2^-} \times Q) \quad (8)$$

where v (mg h^{-1} cm^{-2}) is the yield rate, c (mg/L) is the concentration of NH_3 or NO_2^-, V is the volume of electrolyte in the cathode compartment (50 mL), t is the electrolysis time (1 h), S is the geometric area of the working electrode (1 cm^2), FE (%) is Faradaic efficiency, F is the Faradaic constant (96485 C mol^{-1}), M is the molar mass fraction (g/mol), Q (C) is the total charge passing the electrode.

The gas generated from the closed electrolytic cell was connected with a gas chromatograph (GC) to monitor the gaseous products yield. The GC analysis was carried out on GC-7920 (China Education Au-light Co.) with thermal conductivity detector and Ar carrier gas. The volume of generated gas was analyzed every 10 minutes. The Faradaic efficiency (FE) for hydrogen (H_2) can be calculated according to the following relationship:

$$FE = 2 \times F \times n_{H_2}/Q \quad (9)$$

where n_{H2} (mol) is the calculated amount of hydrogen from the calibration with the peak area of standard H_2 gas.

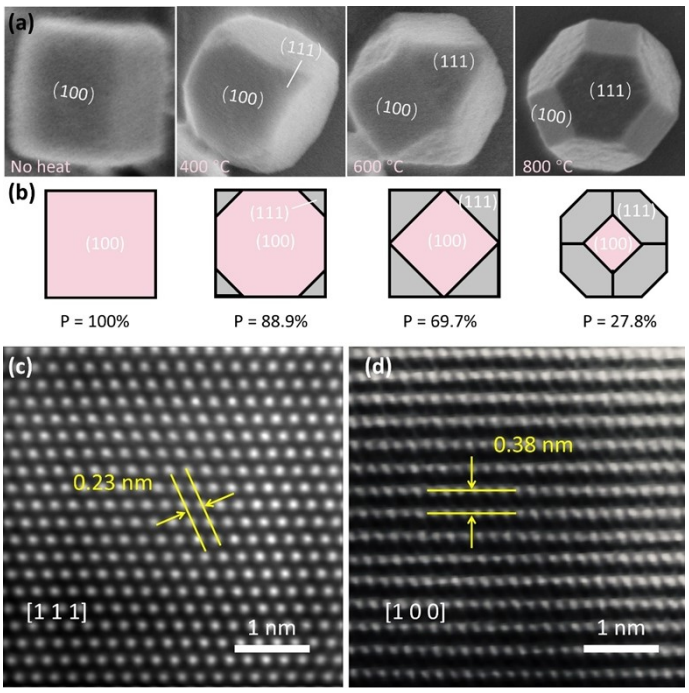

Figure S1. (a) SEM images of the Ga-Cu_3N catalysts synthesized under different transient heating temperatures. (b) the corresponding sketch from the view of the (100) facet. ($P = \frac{S_{(100)}}{S_{(100)} + S_{(111)}}$, S(100) and S(111) are respectively the exposed area of (100) and (111) facets). (c, d) Aberration-corrected HAADF-STEM image of (111) and (100) facet for Ga-Cu_3N prepared at transient heating temperature of 800 °C.

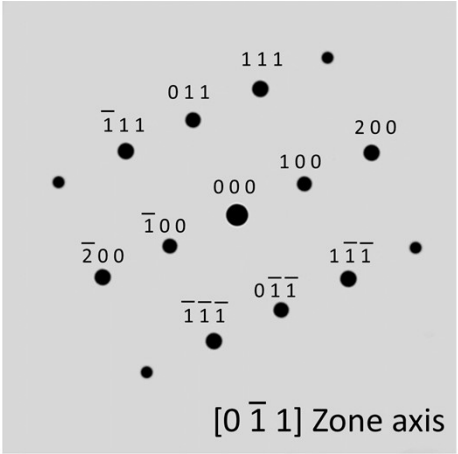

Figure S2. The simulated SAED pattern of Ga-Cu_3N along the crystal zone axis [0 $\bar{1}$ 1] using software crystalmaker with optimized Ga-Cu_3N cif file.

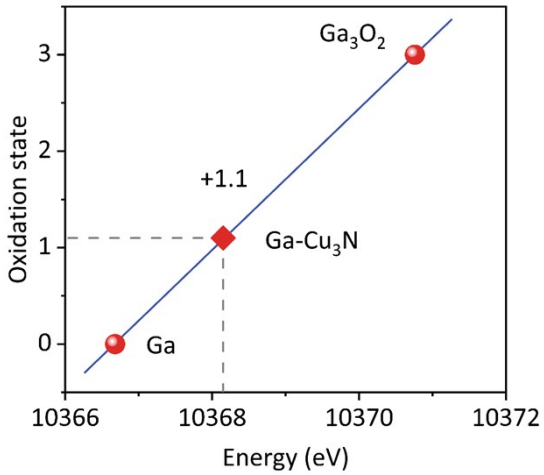

Figure S3. Oxidation state of various gallium species obtained from Ga K-edge XANES.

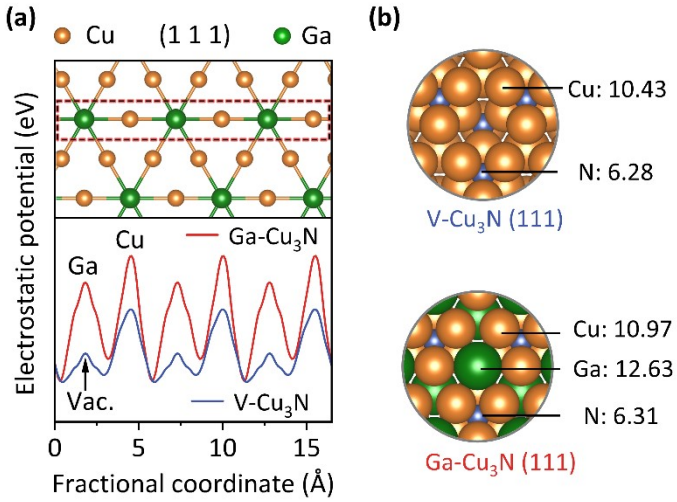

Figure S4. The changes of (a) surface electrostatic potential and (b) Bader charge after Ga doping.

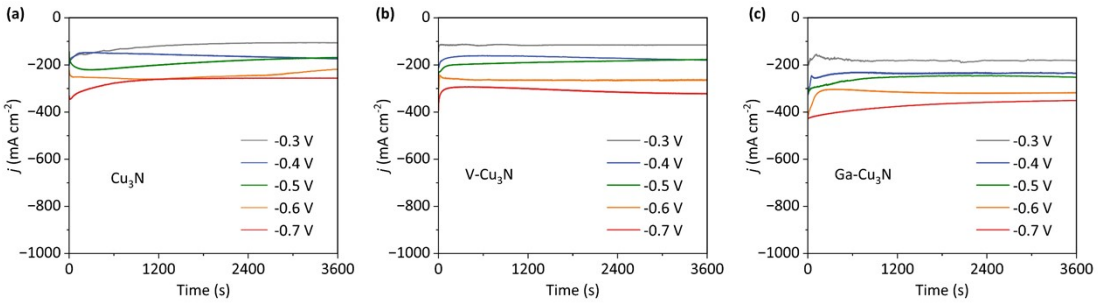

Figure S5. I-t curves of (a) Cu_3N, (b) V-Cu_3N and (c) Ga-Cu_3N for NitRR tests at various potentials in 1 h.

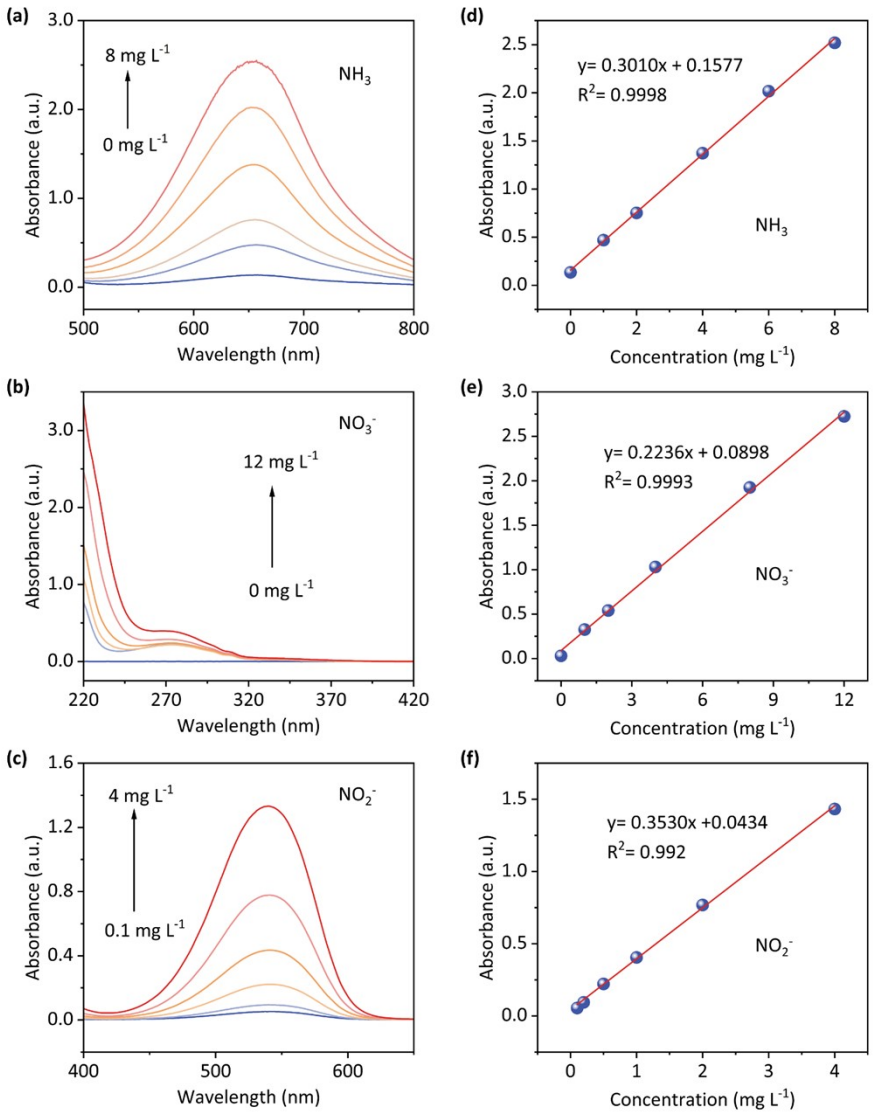

Figure S6. UV-Vis curves of (a) NH_3, (b) NO_3^- and (c) NO_2^- standards with different concentration, and the corresponding linear standard curve (d, e, f).

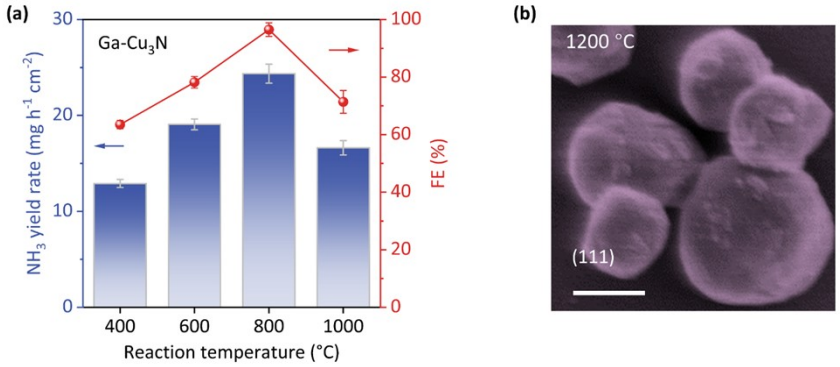

Figure S7. (a) NH_3 yield rate and FE for Ga-Cu_3N catalysts prepared under different transient heating temperatures at -0.6 V vs. RHE. (b) The SEM image of Ga-Cu_3N catalysts prepared under 1000 °C.

Note: As seen in Figure S7a, the Ga-Cu_3N synthesized in 800 °C could achieved highest NH_3 yield (24.36 mg h^{-1} cm^{-2}) and FE (96.48%). It is due to that the low heating temperature was not conducive to the exposure of the (111) crystal plane and the Ga deposition on atomic vacancy. Additionally, the high reaction temperature (≥ 1000 °C) might induce lattice expansion and destroy crystal stability (Figure S7b), thus weakening catalytic performance.

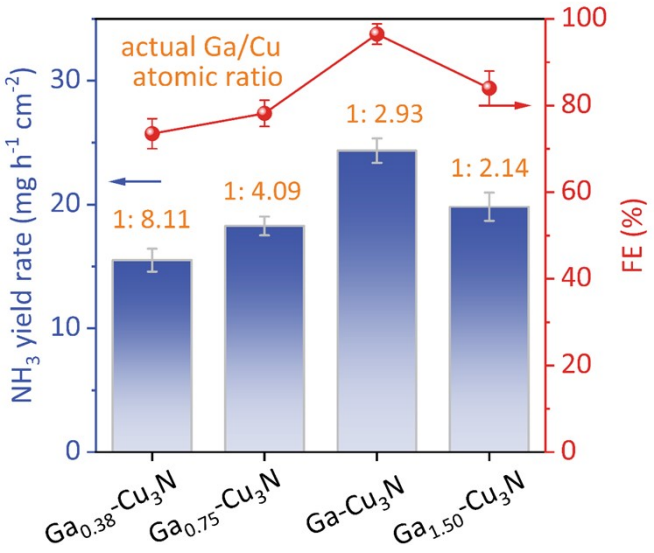

Figure S8. NH_3 yield rate and FE for Ga-Cu_3N catalysts with different Ga/Cu atomic ratio.

Note: We obtained series of Ga-Cu_3N catalysts with different Ga/Cu atomic ratio via changing the added gallium amount (Test S2). Then, we tested their eNitRR activity using the chrono amperometry mode at -0.6 V vs. RHE. As seen in Figure S8 and Table S2, the highest catalytic activity was obtained when the Ga/Cu atomic ratio was 1: 2.93. This ratio was very close to the ratio of atomic vacant sites and Cu sites (1: 3) in ReO_3-type antiperovskite [17,18], which demonstrated that the Ga atoms occupying the atomic vacancy can obviously accelerate eNitRR kinetics. The catalytic activity declined when Ga/Cu ratio increasing to 1:2.14, which can be explained by that excessive Ga atoms formed clusters on the surface and suppressed intermediates reduction on Cu sites in NitRR.

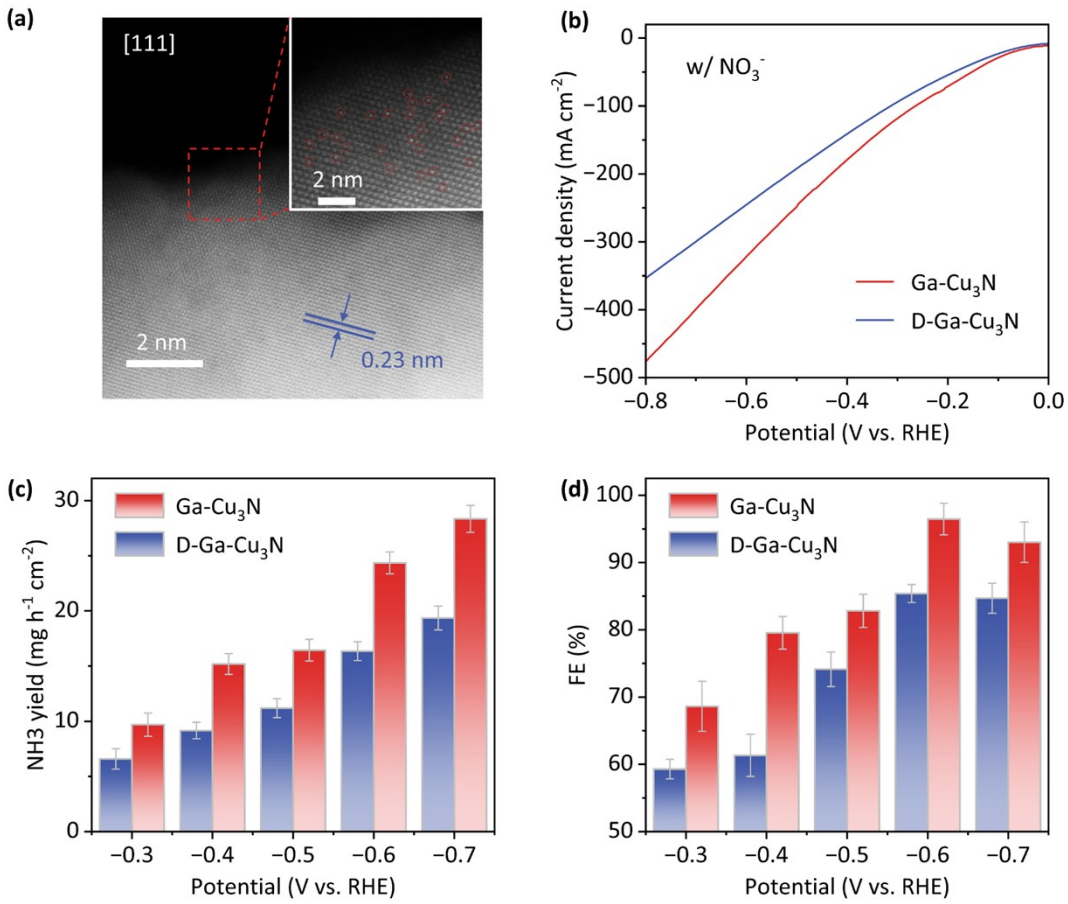

Figure S9. (a) Aberration-corrected HAADF-STEM image of D-Ga-Cu_3N sample. Comparison on (b) Polarization curve, (c) NH_3 yield rate, and (d) Faradaic efficiency of Ga-Cu_3N and D-Ga-Cu_3N catalysts.

Note: The HAADF-STEM image of D-Ga-Cu_3N (Figure S9a) exhibited that the Gallium atoms were unevenly distributed on the (111) crystal plane in the form of single atoms, forming a disordered interface. It is might because that the atom deposition occurred after the atomic vacancy formed, which is hard to occupy all the vacant sites in V-Cu_3N. On the contrary, the atomic vacancy generation and Ga deposition was almost simultaneous in the transient thermal synthesis of Ga-Cu_3N (reaction time: 2s), which is easier to form uniform and ordered reaction crystal planes. The comparison on polarization curve (Figure S9b) disclosed that D-Ga-Cu_3N

revealed smaller current density than Ga-Cu_3N under the same potential. It demonstrated the relatively poor eNitRR activity of D-Ga-Cu_3N, which can be also verified by lower NH_3 yield and Faraday efficiency (Figure S9c and S9d). This result can be explained by that the Ga and Cu established regular and ordered coordination on the Ga-Cu_3N surface with shortest average atomic distance, contributing to that the *H generated from Ga site is more efficient to transfer into the eNitRR intermediates on Cu site.

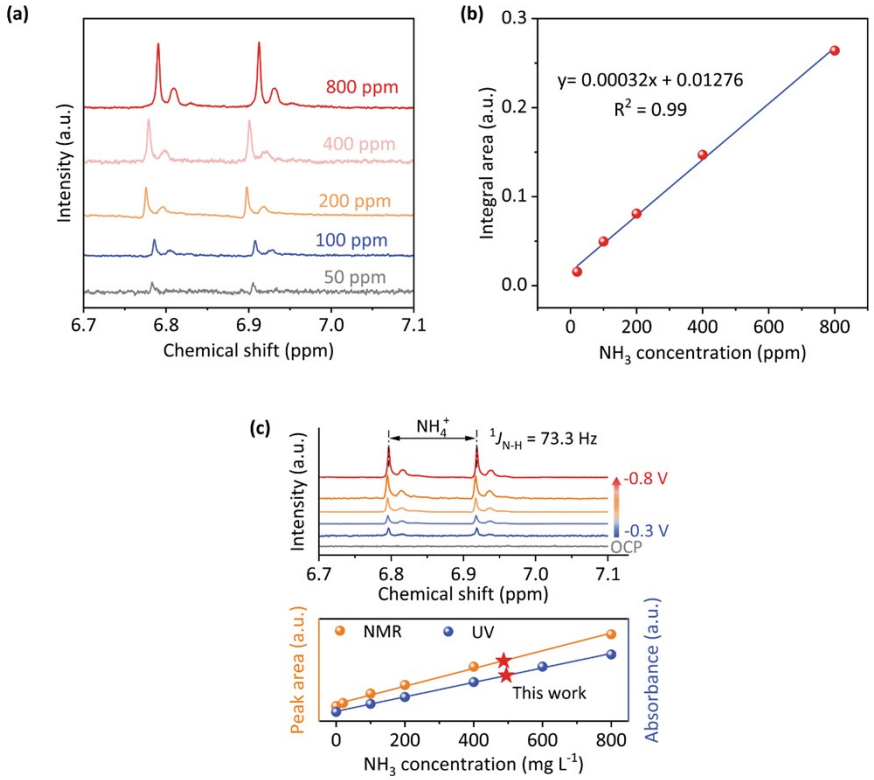

Figure S10. (a) ^{1}H NMR spectra of the $^{15}NH_4Cl$ standards with different content. (b) The corresponding linear standard curve between concentration and peak area. (c) ^{1}H NMR spectra of the electrolyte after reaction using $^{15}NO_3^-$ as the nitrogen source and the calculated concentration comparison with UV method.

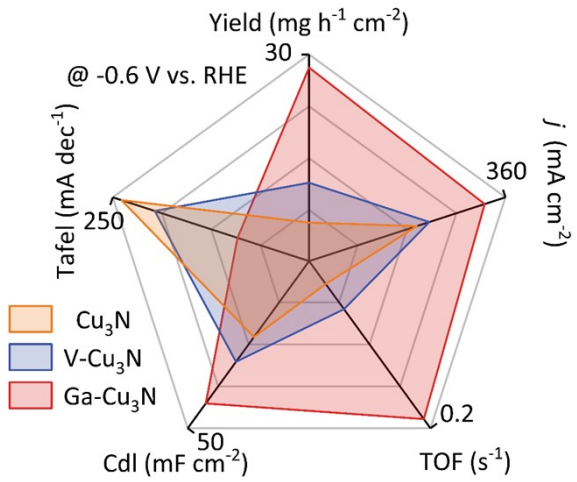

Figure S11. Comprehensive comparison for electrochemical properties of three catalysts.

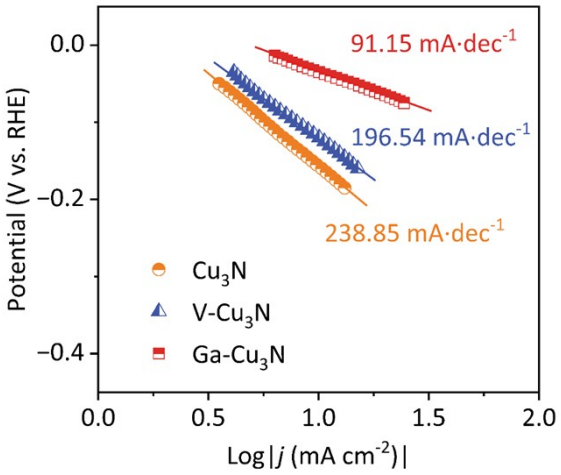

Figure S12. The obtained Tafel slope from of LSV curves for three catalysts.

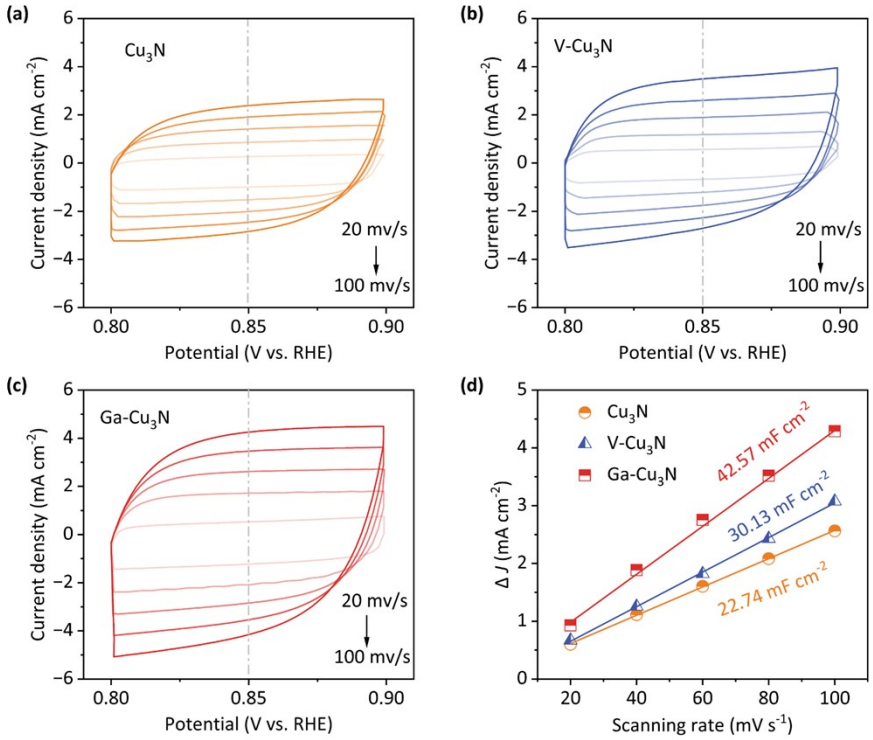

Figure S13. CV curves for (a) Cu_3N, (b) V- Cu_3N, and (c) Ga-Cu_3N from 0.8 to 0.9 V versus RHE with various scan rates. (d) Corresponding derived double layer capacitance (Cdl) of samples.

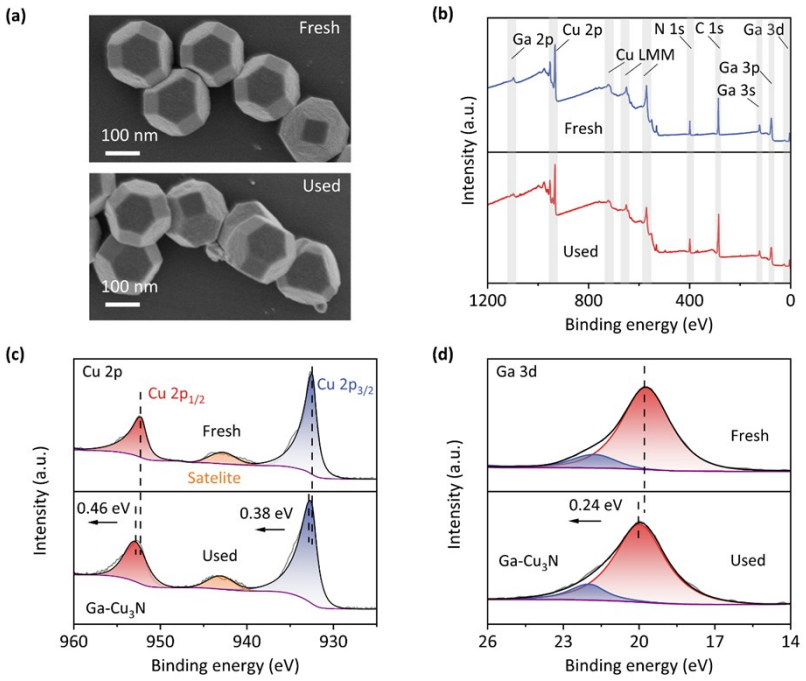

Figure S14. Comparison of (a) SEM, (b) XPS survey spectra, (c) Cu 2p and (d) Ga 3d spectra of Ga-Cu_3N before and after cyclic electrocatalytic tests.

Note: Figure S14a clearly revealed the morphology of the catalyst (peeling from carbon paper by ultrasonic) before and after electrocatalytic ammonia synthesis. It can be seen that the Ga-Cu_3N particles can still maintain the truncated octahedron structure with little deformation after cyclic tests. Moreover, the corresponding XPS spectra comparison (Figure S14b) demonstrates distinguishable element characteristic peaks with no obvious structural deterioration occurred, further proving the stability of the Ga-Cu_3N catalyst in ammonia synthesis. Additionally, the main peak of Cu 2p and Ga 3d in Ga-Cu_3N are both slightly shifted towards high energy direction (Figure S14c and d), suggesting their electron release in the reaction of nitrate reduction and active hydrogen generation, respectively.

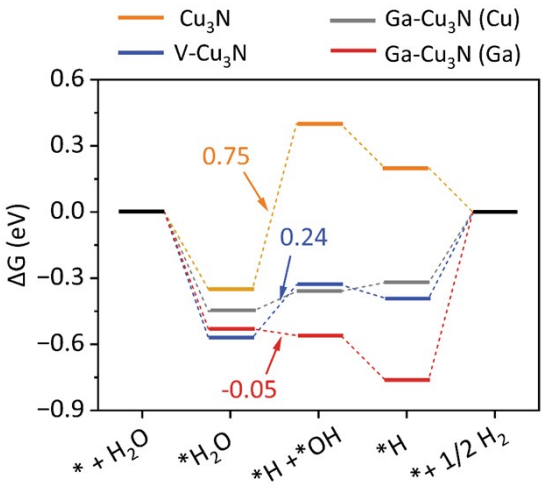

Figure S15. Free energy diagram for H_2O dissociation and *H generation on different sites.

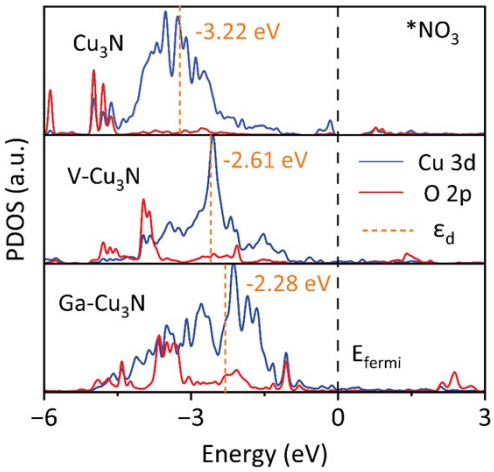

Figure S16. Partial density of states of NO_3^- adsorbed on catalysts. (ε_d: d band center)

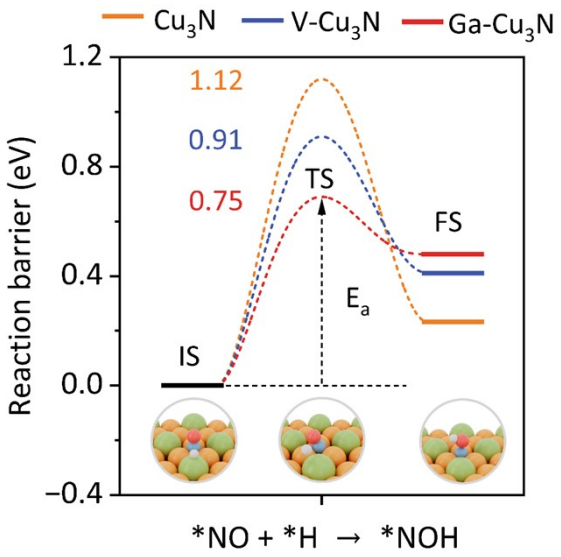

Figure S17. The reaction barrier of the step (*NO + *H →*NOH), accompanied by structures of the initial, transition and final states along reaction.

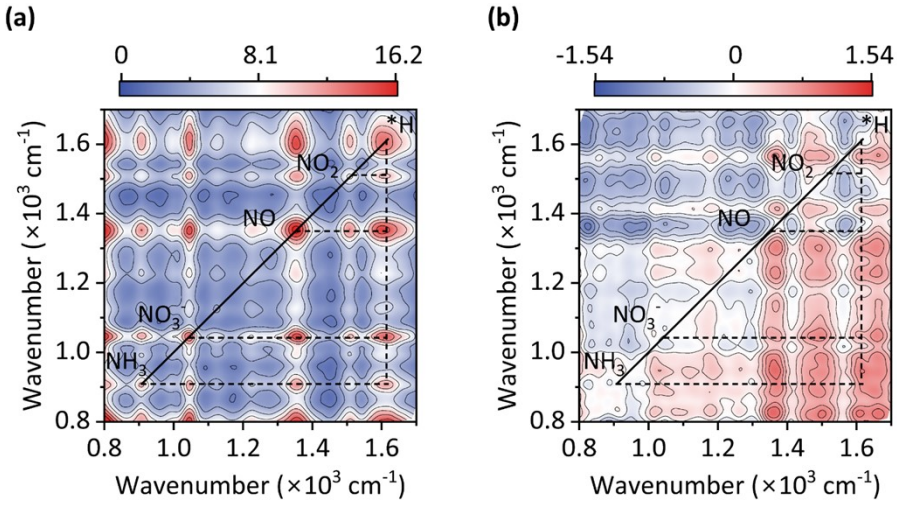

Figure S18. (a) Synchronous and (b) Asynchronous 2D correlation maps generated from in-situ Raman spectra for NitRR using Ga-Cu_3N in the range of 800-1700 cm^{-1}.

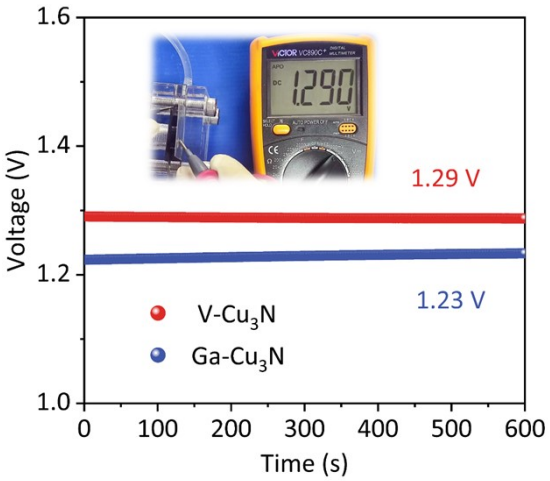

Figure S19. Open circuit voltages from chrono voltage modes.

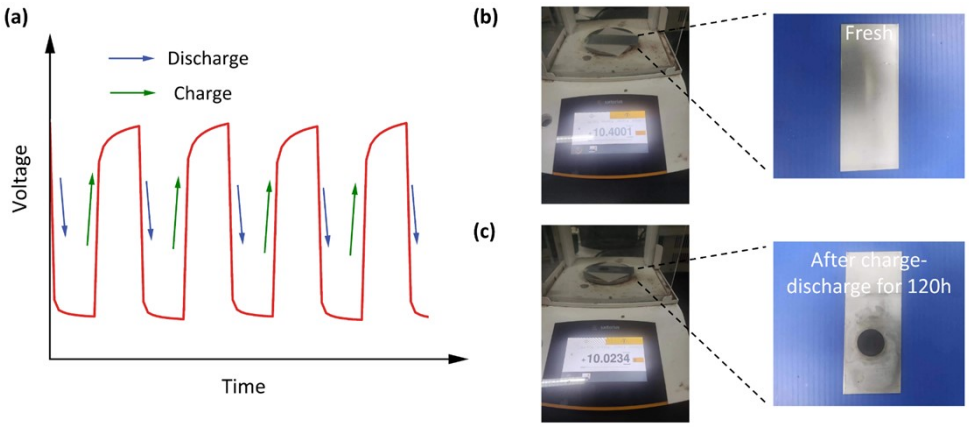

Figure S20. (a) Charge and discharge diagram. Digital photo of the (b) fresh zinc flake and (c) used zinc flake after charge-discharge tests for 120 h.

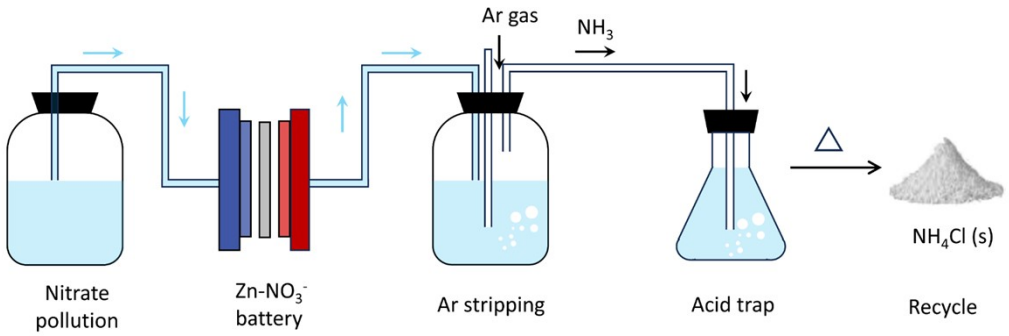

Figure S21. Schematic diagram of ammonia recovery unit coupled with Zn-NO_3^- battery.

Table S1. Ga K-edge EXAFS curve-fitting parameters for Ga-Cu_3N.

Path	N	R (Å)	σ^2 (10^{-3} $Å^{-2}$)	ΔE_0	R-factor
Ga-Cu	5.9±0.2	2.18±0.02	5.9±0.37	4.7±0.2	0.035

N: coordination numbers;

R: distance between absorber and backscatter atoms;

σ^2: Debye-Waller Factor;

ΔE_0: inner potential correction;

R-factor: goodness of the fit.

Table S2. Inductively coupled plasma mass spectrometry results for all catalyst and the normalized NH_3 yield rate on Cu sites at -0.6 V vs. RHE.

Sample	Cu wt%	Ga wt%	Ga/Cu atomic ratio	NH_3 yield (mg h^{-1} cm^{-2})	Normalized yield (mmol h^{-1} mg_{Cu}^{-1})
Cu_3N	92.43	—	—	4.92	1.57
V-Cu_3N	90.64	—	—	9.93	3.22
Ga-Cu_3N	68.40	25.56	1: 2.93	24.36	10.47
$Ga_{0.38}$-Cu_3N	82.70	11.16	1: 8.11	15.51	5.52
$Ga_{0.75}$-Cu_3N	74.48	19.9	1: 4.09	18.27	7.21
$Ga_{1.50}$-Cu_3N	63.06	32.27	1: 2.14	19.82	9.25
D-Ga-Cu_3N	69.32	26.89	1: 2.84	16.35	6.94

Table S3. Signs of main cross-peak (ν_1, ν_2) in the synchronous (Φ) and asynchronous (Ψ) maps of *in-situ* Raman spectrum (Figure S10) for Ga-Cu_3N.

ν_2 / ν_1	$*NO_3^-$	$*NO_2^-$	*NO	$*NH_2$	$*NH_3$
*H	(+, +)	(+, +)	(+, +)	(+, +)	(+, +)

Herein, according to the Noda's rule [19], the change occurred at the position ν_1 is prior to that at ν_2 if Φ (ν_1, ν_2) and Ψ (ν_1, ν_2) have the same sign. The order is reversed if Φ (ν_1, ν_2) and Ψ (ν_1, ν_2) are with opposite sign.

Table S4. Comparisons with reported bifunctional catalysts on eNitRR half reaction and Zn-NO_3^- battery performance.

eNitRR	NH_3 yield ($mg\ h^{-1}\ cm^{-2}$)	FE (%)	Durability (h)	Ref.
Ga-Cu_3N	**24.36**	**96.48**	**120**	**This Work**
i-Ag-Co_3O_4	4.31	94.30	10	[20]
Pd-TiO_2	1.12	93.10	12	[21]
MP-Cu	3.80	97	12	[22]
Ni/Co-MOF	6.63	99.70	16	[23]
Ni_1Cu-SAA	5.55	100	8.8	[24]
CuTABQ	4.67	97.7	10	[25]
Fe/Ni_2P	4.17	94.30	10	[26]
$NiCo_2O_4$	16.5	99	16	[27]
Fe_2TiO_5	2.48	96.60	24	[28]

Zn-NO_3^- battery	NH_3 yield ($mg\ h^{-1}\ cm^{-2}$)	FE (%)	OCV (V)	Power ($mW\ cm^{-2}$)	Ref.
Ga-Cu_3N	**3.62**	**94.80**	**1.69**	**23.85**	**This Work**
i-Ag-Co_3O_4	0.72	91.4	1.32	2.56	[20]
Pd-TiO_2	0.54	81.3	0.81	0.87	[21]
MP-Cu	1.29	93	1.27	7.56	[22]
Ni/Co-MOF	1.125	99.40	1.47	3.66	[23]
Ni_1Cu-SAA	2.108	88.6	1.51	12.7	[24]
CuTABQ	1.17	98.4	0.75	12.3	[25]
Fe/Ni_2P	0.38	85	1.22	3.25	[26]
$NiCo_2O_4$	0.824	96.10	1.3	3.94	[27]
Fe_2TiO_5	0.78	87.6	1.5	5.6	[28]

Reference

1 M. Parvizian, A. Duràn Balsa, R. Pokratath, C. Kalha, S. Lee, D. Van den Eynden, M. Ibáñez, A. Regoutz and J. De Roo, *Angew. Chem. Int. Ed.*, 2022, **61**, e202207013.

2 D. X. Luong, K. V. Bets, W. A. Algozeeb, M. G. Stanford, C. Kittrell, W. Chen, R. V. Salvatierra, M. Ren, E. A. McHugh, P. A. Advincula, Z. Wang, M. Bhatt, H. Guo, V. Mancevski, R. Shahsavari, B. I. Yakobson and J. M. Tour, *Nature*, 2020, **577**, 647–651.

3 J. Hafner, *J. Comput. Chem.*, 2008, **29**, 2044–2078.

4 V. Wang, N. Xu, J.-C. Liu, G. Tang and W.-T. Geng, *Comput. Phys. Commun.*, 2021, **267**, 108033.

5 S. Maintz, V. L. Deringer, A. L. Tchougréeff and R. Dronskowski, *J. Comput. Chem.*, 2016, **37**, 1030–1035.

6 G. Henkelman, B. P. Uberuaga and H. Jónsson, *J. Chem. Phys.*, 2000, **113**, 9901–9904.

7 M. Tuckerman, K. Laasonen, M. Sprik and M. Parrinello, *J. Chem. Phys.*, 1995, **103**, 150–161.

8 B. H. Toby and R. B. Von Dreele, *J. Appl. Crystallogr.*, 2013, **46**, 544–549.

9 M. J. Hÿtch, E. Snoeck and R. Kilaas, *Ultramicroscopy*, 1998, **74**, 131–146.

10 B. Ravel and M. Newville, *J. Synchrotron Radiat.*, 2005, **12**, 537–541.

11 W. Gao, K. Xie, J. Xie, X. Wang, H. Zhang, S. Chen, H. Wang, Z. Li and C. Li, *Adv. Mater.*, 2023, **35**, 2202952.

12 K. W. Knehr and E. C. Kumbur, *Electrochem. Commun.*, 2011, **13**, 342–345.

13 H. Xu, Y. Ma, J. Chen, W. Zhang and J. Yang, *Chem. Soc. Rev.*, 2022, **51**, 2710–2758.

14 J. Yi, P. Liang, X. Liu, K. Wu, Y. Liu, Y. Wang, Y. Xia and J. Zhang, *Energy Environ. Sci.*, 2018, **11**, 3075–3095.

15 X. Liu, Y. Yuan, J. Liu, B. Liu, X. Chen, J. Ding, X. Han, Y. Deng, C. Zhong and W. Hu, *Nat. Commun.*, 2019, **10**, 4767.

16 X. Wei, X. Wen, Y. Liu, C. Chen, C. Xie, D. Wang, M. Qiu, N. He, P. Zhou, W. Chen, J. Cheng, H. Lin, J. Jia, X.-Z. Fu and S. Wang, *J. Am. Chem. Soc.*, 2022, **144**, 11530–11535.

17 D. M. Borsa, S. Grachev, C. Presura and D. O. Boerma, *Appl. Phys. Lett.*, 2002, **80**, 1823–1825.

18 Y. Wang, H. Zhang, J. Zhu, X. Lü, S. Li, R. Zou and Y. Zhao, *Adv. Mater.*, 2020, **32**, 1905007.

19 I. Noda, *Vib. Spectrosc.*, 2012, **60**, 146–153.

20 S. Wu, Y. Jiang, W. Luo, P. Xu, L. Huang, Y. Du, H. Wang, X. Zhou, Y. Ge, J. Qian, H. Nie and Z. Yang, *Adv. Sci.*, 2023, 2303789.

21 Y. Guo, R. Zhang, S. Zhang, Y. Zhao, Q. Yang, Z. Huang, B. Dong and C. Zhi, *Energy Environ. Sci.*, 2021, **14**, 3938–3944.

22 W. Wen, P. Yan, W. Sun, Y. Zhou and X.-Y. Yu, *Adv. Funct. Mater.*, 2023, **33**, 2212236.

23 J. Ma, Y. Zhang, B. Wang, Z. Jiang, Q. Zhang and S. Zhuo, *ACS Nano*, 2023, **17**, 6687–6697.
24 J. Cai, Y. Wei, A. Cao, J. Huang, Z. Jiang, S. Lu and S.-Q. Zang, *Appl. Catal. B Environ.*, 2022, **316**, 121683.
25 R. Zhang, H. Hong, X. Liu, S. Zhang, C. Li, H. Cui, Y. Wang, J. Liu, Y. Hou, P. Li, Z. Huang, Y. Guo and C. Zhi, *Angew. Chem. Int. Ed.*, **n/a**, e202309930.
26 R. Zhang, Y. Guo, S. Zhang, D. Chen, Y. Zhao, Z. Huang, L. Ma, P. Li, Q. Yang, G. Liang and C. Zhi, *Adv. Energy Mater.*, 2022, **12**, 2103872.
27 Q. Liu, L. Xie, J. Liang, Y. Ren, Y. Wang, L. Zhang, L. Yue, T. Li, Y. Luo, N. Li, B. Tang, Y. Liu, S. Gao, A. A. Alshehri, I. Shakir, P. O. Agboola, Q. Kong, Q. Wang, D. Ma and X. Sun, *Small*, 2022, **18**, 2106961.
28 H. Du, H. Guo, K. Wang, X. Du, B. A. Beshiwork, S. Sun, Y. Luo, Q. Liu, T. Li and X. Sun, *Angew. Chem.*, 2023, **135**, e202215782.